Effects of Symmetry Breaking and Conductive Contact on the Plasmon Coupling in Gold Nanorod Dimers

Liane S. Slaughter,[†,⊥] Yanpeng Wu,[‡,⊥] Britain A. Willingham,[†,⊥] Peter Nordlander,[‡,§,⊥,*] and Stephan Link[†,§,⊥,*]

[†]Department of Chemistry, [‡]Department of Physics, [§]Department of Electrical and Computer Engineering, and [⊥]Laboratory for Nanophotonics, Rice University, Houston, Texas 77005

ABSTRACT We have explored the consequences of symmetry breaking on the coupled surface plasmon resonances in individual dimers of gold nanorods using single-particle dark-field scattering spectroscopy and numerical simulations. Pairs of chemically grown nanorods can exhibit wide variation in sizes, gap distances, and relative orientation angles. The combination of single-particle spectroscopy and theoretical analysis allowed us to discern the effects of specific asymmetry-inducing parameters one at a time. The dominant influence of symmetry breaking occurred for longitudinal resonances in strongly coupled nanorods in linear end-to-end configurations. In particular, we found that the normally dark antibonding dimer mode becomes visible when the sizes of the two nanorods are different. In addition, we observed a conductively coupled plasmon mode that was red-shifted by at least 250 nm from the bonding plasmon mode for the corresponding nontouching geometry. Gaining detailed insight into how symmetry breaking influences coupled surface plasmon resonances of individual nanorod dimers is an important step toward the general understanding of the optical properties of assemblies of chemically synthesized nanorods with unavoidable irregularities in size and orientation.

KEYWORDS: gold nanorods · surface plasmon resonance · nanoparticle dimers · plasmon hybridization · single-particle spectroscopy · plasmon coupling

A plethora of studies have illuminated the diverse optical properties of gold and silver nanostructures. The sensitivity of the localized surface plasmon resonances (LSPRs) to size, shape, and surrounding media provides multiple avenues for tuning the way nanoparticles interact with light in imaging and sensing systems.[1−4] The number of possibilities for exploiting the LSPRs further increases when taking advantage of the interactions between the LSPRs for particles in close proximity. In nanoparticle dimers, the red shift of the LSPR maximum to longer wavelengths can serve as a plasmonic ruler, especially useful for measuring biomolecular distances.[5−7] In addition, the strong local enhancement of the electric field between the particles is beneficial to surface-enhanced spectroscopies to a greater extent than the field enhancement around single particles.[8−10] The spectral changes from the LSPR of isolated nanoparticles are most easily observable in the closely coupled regime, where the distance between adjacent nanoparticles is on the order of one radius or less.[11−20]

A dimer is also the simplest building block in a nanoparticle waveguide. Chemical synthesis and assembly methods yield one-dimensional arrays of nanoparticles having much smaller separations than what can typically be achieved using electron-beam lithography fabrication methods,[21−23] potentially improving the efficacy of plasmonic waveguides.[24,25] Although chemical synthesis creates nanoparticles with few defects and a very pure plasmonic response, the resulting particles exhibit a distribution of sizes and shapes. Thus, an assembly of such nanoparticles will naturally contain local irregularities in the geometries and spacings among neighboring particles. Such variations will influence the wavelength of the coupled LSPRs, especially if the particles touch each other, allowing the excitation of charge transfer plasmons.[11,26] A recent study of gold heterodimers has already demonstrated the rich variety of properties that arises when the two particles are intentionally mismatched in size or composition.[27] The variety of new phenomena that can occur increases in complexity for dimers consisting of anisotropic particles, such as nanorods where the relative orientation also becomes an important parameter.[2,13,28−33]

The longitudinal LSPR of a nanorod is highly tunable and sensitive to polarization, which enables individual nanorods to act as efficient orientation sensors.[1,34,35] The anisotropic shape and surface chemistry furthermore allow for their oriented assembly.[21,23,36] Despite these potentially advantageous features, the angular degree

*Address correspondence to nordland@rice.edu, slink@rice.edu.

Received for review May 20, 2010 and accepted June 30, 2010.

Published online July 8, 2010. 10.1021/nn1011144

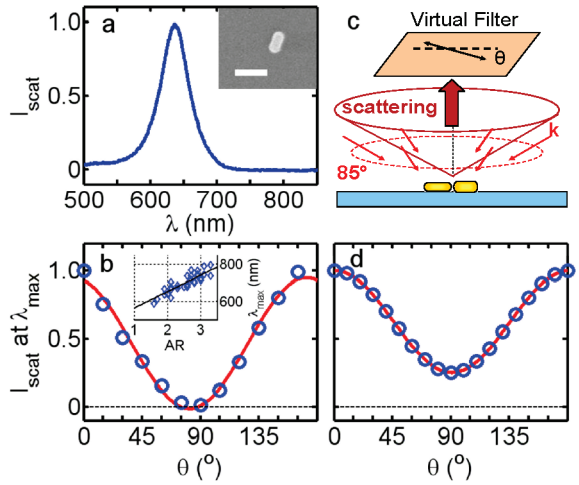

Figure 1. (a) Unpolarized dark-field scattering spectrum and SEM image (inset) of a single gold nanorod with dimensions of (70 × 37) ± 5 nm. The scale bar represents 100 nm. (b) Dependence of the scattering amplitude at 620 nm on the angle of the detected polarization relative to the rod. Inset: Dependence of the maximum of the longitudinal LSPR λ_{max} on the aspect ratio. (c) Schematic of the geometry employed to calculate integrated dark-field scattering in reflection mode in FDTD; θ indicates the angle of the polarization selected by the virtual filter. (d) Simulated dependence of the scattering amplitude at λ_{max} on θ for the rod shown in (a).

of freedom in an assembly of nanorods complicates predicting the interactions of LSPRs even within a simple dimer. To address this issue, correlated scanning electron microscopy (SEM) and single-particle dark-field scattering spectroscopy have been performed for gold nanorod dimers with rods in specific geometries such as side-by-side, end-to-end, as well as L- and T-shaped arrangements.[29] Furthermore, the effect of rotating one rod with respect to the other was investigated for both nanorod dimers that were formed by lithography[31] with separations no smaller than 20 nm as well as for chemically linked nanorods with ~1 nm gaps.[33] While the effects of orientational symmetry breaking have been addressed in these previous studies, to our knowledge, a detailed understanding of the influence of size mismatch on the collective optical properties of nanorod dimers is still missing. Symmetry breaking due to the unequal sizes of the particles composing the dimer is of particular concern for dimers formed from chemically grown nanorods which naturally exhibit a size heterogenity.

We have therefore explored the consequences of incongruities of individual nanorod dimers on their coupled LSPRs using polarization-sensitive single-particle spectroscopy, SEM, plasmon hybridization calculations, and finite-difference time domain (FDTD) computations. The dimers of chemically grown nanorods were formed fortuitously during evaporation from their aqueous solution and therefore exhibited wide variation in mismatched sizes, gap distances, and angles. The FDTD simulations were performed using incidence and scattering geometries that matched the experimental setup of the dark-field scattering microscope. The theoretical analysis of the experimental data allowed us to discern the effect of specific asymmetry-inducing parameters one at a time. Correlating these structural variations with the intensities and peak positions of coupled LSPRs in nanorod dimers is important for understanding how plasmon coupling depends on irregularities that are ubiquitous in assemblies of chemically prepared nanoparticles.

RESULTS AND DISCUSSION

Gold nanorods synthesized in solution using the standard seed-mediated growth method and stabilized with cetyltrimethylammonium bromide (CTAB)[2] were obtained from Nanopartz, Inc. Samples of single nanorods and dimers supported on a patterned glass substrate were prepared by drop casting. We characterized all nanostructures with SEM and dark-field scattering spectroscopy. The unpolarized spectrum of a single nanorod with dimensions of (70 × 37) ± 5 nm and aspect ratio of AR = 1.8 in Figure 1a shows the primary scattering peak occurring at 620 nm. A polarization-sensitive detection scheme allowed us to isolate the longitudinal and transverse nature of the plasmon modes. In Figure 1b, for example, the angle of the detected polarization, θ, is varied relative to the rod's major axis. The maximum intensity at 620 nm occurs for θ = 180° when the polarization is parallel to the major axis of the nanorod, while the intensity at this wavelength becomes zero for perpendicular polarization. As shown in Figure 1a, the transverse LSPR is too weak to be detected in the single-particle spectrum. Both the wavelength of the longitudinal LSPR and absence of the transverse mode in the single-particle scattering spectrum are typical of small rods that fall within the quasi-static limit, where the aspect ratio determines the LSPR energy.[1] The inset of Figure 1b confirms a linear relationship between the wavelength of the longitudinal LSPR and the aspect ratio. Given that the widths of the rods varied from 20 to 35 nm, this trend implies that among the rods studied here the aspect ratio is the most important parameter in governing the LSPR maximum.

In the FDTD calculations, the scattering spectra were calculated by collecting all of the scattered far-field within a cone-shaped domain above the nanostructures defined by the numerical aperture (NA) of the objective[37] and integrating the optical cross sections for all different excitation directions. The incident k-vectors were orientated 85° from the normal to the substrate, consistent with the illumination NA of the objective, and s- and p-polarizations were equally weighted. The calculated scattering therefore represents the average for the different excitation angles, which varied in 15° increments around the cone. We also introduced in the FDTD calculations a virtual polarizer having an angle θ relative to the nanorod to select the polarization com-

ponents of the far-field projected onto the sample plane. This procedure allowed us to calculate both unpolarized and polarization-dependent scattering spectra for direct comparison with the experiments. The calculated scattering intensity at the maximum of the longitudinal dipole mode, λ_{max}, as a function of filter angle θ is shown in Figure 1d. Comparing Figure 1d with the experimentally measured polarization dependence in Figure 1b illustrates that the same $\cos^2(\theta)$ dependence is recovered and that the calculated trend obtained by varying the filter angle is therefore a realistic representation of the experimental excitation and collection geometry. The slight offset from zero intensity for perpendicular polarization in the theoretical calculations (Figure 1d) is caused by numerical errors generated when modeling a spherically symmetric far-field collection area using a virtual filter defined on a Cartesian FDTD grid. Such an offset will therefore also be present in the polarization dependence of the scattering amplitudes for the other nanorod dimer structures such as the end-to-end dimer discussed below.

It is important to mention here that the peak positions calculated in FDTD were not well matched to the experiment unless the CTAB coating and the glass substrate were included. The dielectric constants for glass and CTAB were $\varepsilon = 2.31$ and 4, respectively. The latter was chosen by tuning this value in the simulated spectrum of a single rod to match the experiment. We assumed a thickness of 4 nm for the CTAB bilayer. Although the thickness may vary around the dried particles, our estimate is consistent with previous reports.[38] Simulations performed for individual rods and dimers with and without the substrate consistently demonstrated that the substrate induced a red shift but no other spectral features. In addition, the nanorods were modeled as perfect hemispherically capped cylinders with smooth surfaces. Such an idealization neglects any defect-induced damping likely to be present in the experimental structures. Therefore, all simulated spectra have slightly narrower resonances.

The same experimental and computational strategies were then applied for characterizing plasmon coupling for a dimer of nanorods aligned side-by-side. Figure 2a plots the scattering spectrum of the dimer shown in Figure 2c and the scattering spectra of individual rods with aspect ratios similar to those in the dimer. Note that the individual rods did not necessarily have the same dimensions as the rods making up the dimer. The inset of Figure 1b, however, shows that the aspect ratio is the primary variable affecting the LSPR wavelength for these rods. The dimer displays one resonance peak at 620 (645) nm observed in the experiment (simulation), which is blue-shifted relative to the peaks of each individual rod at 705 (679) nm and 680 (679) nm. These spectra are consistent with the FDTD result in Figure 2b. The electric field enhancement and charge distributions depicted in Figure 2d,e show that

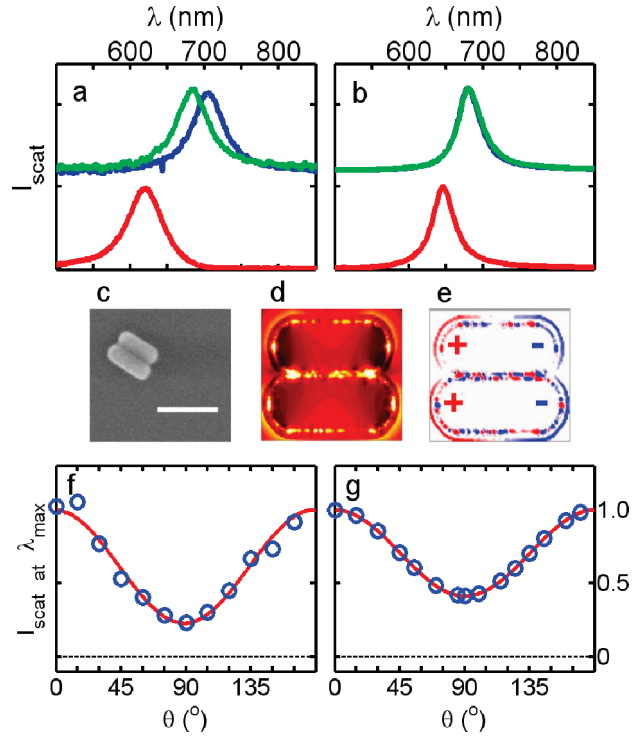

Figure 2. (a) Unpolarized dark-field scattering spectra of a dimer (red) with rods aligned side-by-side and individual rods with aspect ratios comparable to those composing the dimer (green and blue). (b) Integrated dark-field scattering spectra simulated by FDTD of the dimer (red) and the individual rods composing the dimer (blue and green) without the polarizing virtual filter. (c) SEM image of the side-by-side dimer measured in (a) and simulated in (b) showing that the dimer consists of gold nanorods with dimensions of (70 × 25) ± 5 nm (top rod) and (76 × 28) ± 5 nm (bottom rod) and aspect ratios of 2.8 and 2.7, respectively. The scale bar indicates 100 nm. (d,e) Calculated electric field enhancement and charge distribution from FDTD, respectively. (f) Measured and (g) simulated intensity at 620 nm showing how the side-by-side dimer peak depends on the detected polarization angle θ.

the dipole modes of the individual nanorods are aligned parallel to each other.[39,40] This antibonding interaction has higher energy compared to the bonding mode with its antiparallel dipolar alignment.[28,41] This finding is consistent with a mode analysis performed within the framework of plasmon hybridization theory.[42,43] The lower energy bonding mode with its oppositely aligned dipoles has no total dipole moment and is thus unobservable. The higher energy antibonding mode has a net dipole oriented along the long axes of the rods, consistent with the fitted $\cos^2(\theta)$ polarization dependences in Figure 2f,g and the fact that the scattered light intensity reaches a maximum when the polarization is parallel to the long axes of the rods. The small but nonzero intensity in Figure 2f,g for polarization perpendicular to the major dimer axis suggests that plasmon coupling in this side-by-side dimer also involves, although to a much smaller extent, other higher order multipolar plasmon modes with transverse character.[43]

In Figure 3, we show the experimental (a) and theoretical (b) scattering spectra for a nanorod heterodimer

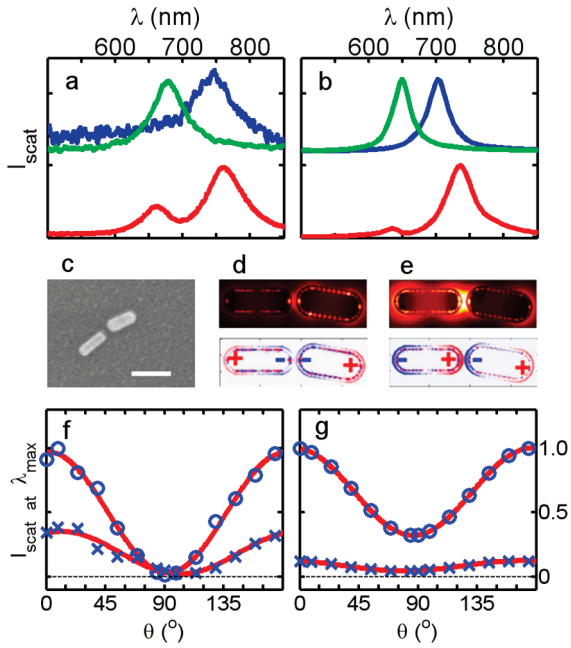

Figure 3. (a) Unpolarized dark-field scattering spectra of an end-to-end dimer (red) and individual rods with aspect ratios comparable to those composing the dimer (green and blue). (b) Integrated dark-field scattering spectra simulated by FDTD of the dimer (red) and the individual rods composing the dimer (blue and green) without a polarizing virtual filter. (c) SEM image of the end-to-end dimer measured in (a) and simulated in (b) showing that the dimer consists of gold nanorods with dimensions of (80 × 29) ± 5 nm (left rod) and (74 × 32) ± 5 nm (right rod) and aspect ratios of 2.8 and 2.3, respectively. The scale bar represents 100 nm. (d,e) Electric field enhancement (top) and charge distribution (bottom) calculated by FDTD at the maxima for the short (secondary) and long (primary) wavelength scattering peaks, respectively. (f) Measured and (g) simulated intensity at the maximum of the primary (circles) and secondary (crosses) scattering resonances showing how the modes illustrated in (d) and (e) depend on the detected polarization angle θ.

in an end-to-end configuration with an approximate separation of 12 nm according to the SEM image. The spectra of individual rods with similar aspect ratios as those which compose the dimer are also shown in Figure 3a,b. The individual rod resonances occur at 745 (700) nm for AR = 2.8 and 680 (650) nm for AR = 2.3 in the experiment (simulation). The intense lower energy peak in the dimer spectrum, which occurs near 760 nm in the experiment and near 740 nm in the simulation, occurs at a longer wavelength than either of the longitudinal dipole LSPRs for the individual particles. In contrast, the weaker higher energy peak at 660 (635) nm in the experimental (simulated) spectrum is blueshifted compared to the longitudinal LSPRs of both individual nanorods. Thus, both resonances in the scattering spectrum of the end-to-end dimer result from near-field interactions between the rods and cannot be accounted for by a superposition of the scattering from the constituent particles.

The FDTD field and charge plots in Figure 3d,e show that the peaks result mainly from the interaction of the longitudinal nanorod dipole modes. The strong enhancement of the electric field within the gap and the charge plot at 735 nm in Figure 3e demonstrate that this mode is the bonding dimer mode with a parallel alignment of the dipoles of each nanorod. The field and charge plots for 635 nm in Figure 3d reveal an antiparallel alignment of the individual dipoles, which is characteristic of the antibonding dimer mode. The experimental (Figure 3f) and simulated (Figure 3g) polarization dependences for the two modes confirm that both are longitudinal in nature.

For a linear homodimer, the longitudinal antibonding mode would be dark because antiparallel dipoles result in no net dipole for the dimer. To understand why the antibonding mode appears in the spectra, we then analyzed the effects of different factors that break the symmetry. The experimental and simulated conditions differed from the perfectly symmetric case, and two obvious sources of broken symmetry are present: the size heterogeneity between the two nanorods and the slight angular offset of ~10° relative to a linear alignment.

In the FDTD simulations shown in Figure 4, we investigate both the effect of relative orientation of the nanorods (a) and size mismatch (b). The results demonstrate that the major factor governing the intensity of the antibonding mode is size heterogeneity. The homodimers in Figure 4a consisted of two identical (80 × 30) nm rods (AR = 2.7) with a gap size maintained at 10 nm, and the second rod was given an offset angle, δ, as a measure of the deviation from the linear geometry. For the bent dimer, only a bonding mode is present for $\delta < 45°$. Comparing these results to Figure 3, we conclude that it is unlikely that the offset angle of $\delta = 10°$ in the experiment is the primary factor imparting brightness to the antibonding mode.

Figure 4b shows the FDTD results for heterodimers consisting of nanorods with different sizes. The geometry of the dimers is defined by the variable $\beta = AR_2/AR_1$ where the subscripts 1 and 2 refer to the left and right rods. The spectrum for the linear homodimer ($\beta = 1$) shows only one peak, the bonding mode. As the value of β increases, this mode red shifts and the antibonding mode begins to appear with increasing intensity around 680 nm. For the linear heterodimer, the net dipole moment of the antibonding mode is nonzero because the individual nanoparticle dipoles have different magnitudes. This renders the antibonding mode bright and excitable. Recently, Chu *et al.* observed the antibonding mode for a dimer consisting of gold nanorods with similar size ($\beta \sim 1.1$) and an angular offset of $\delta = 18°$ using electron energy loss spectroscopy (EELS).[44] However, EELS is sensitive to both bright and dark plasmons independent of the value for δ, and their calculated optical spectra for this dimer showed that the antibonding mode is indeed more than an order of magnitude lower in intensity than the bonding mode. Also, Shao *et al.* have studied single dimers of gold

nanorods having a wide range of offset angles using dark-field spectroscopy and found that the scattering spectra for dimers with $\delta = 40-140°$ showed two peaks while angles closer to a linear or parallel arrangement did not induce a second observable mode.[33] Both of these studies are in good agreement with our results in Figure 4.

The plasmonic interaction between two arbitrarily sized and aligned nanorods can be calculated using the plasmon hybridization method.[28,29,43] In this approach, which is exact in the quasistatic limit, the plasmon modes of the nanorod dimer are expressed as linear combinations of the multipolar plasmon modes of each nanorod (primitive modes). For an individual nanorod, plasmon modes of different multipolar symmetry cannot interact. However, in the dimer geometry, multipolar plasmons of different orders on different particles can interact. These complex interactions result in hybridized dimer modes with mixed multipolar compositions.

Figure 5 shows an application of plasmon hybridization to the end-to-end nanorod dimer discussed in Figures 3 and 4. The nanorods are modeled as prolate spheroids of uniform electron density. The dimensions of the dimer have been scaled down to an overall size that is within the quasistatic regime. The insets show the evolution of the longitudinal bonding and antibonding eigenvalues as a function of the gap size for the mode orders $l = 1-3$. The scaled interparticle separation that corresponds to the heterodimer discussed in Figure 3 is $d_{gap} = 2.4$ nm and is indicated by the dashed line in the inset of Figure 5. Figure 5a depicts the extinction spectrum of a linear homodimer with each particle having an AR = 2.5, similar to the average for the experimental nanorod sample. The calculated spectrum shows only one resonance, the bonding dipolar mode (green) at 570 nm (2.19 eV). The dipolar antibonding mode (red) remains dark, with an energy between the bonding dipolar and quadrupolar modes.

In contrast, for the heterodimer (Figure 5b) with $\beta = 1.2$, the antibonding dimer mode is now visible on the blue side of the bonding peak. The charge distribution at 550 nm (2.25 eV) in the inset of Figure 5b confirms the assignment of the antibonding mode. A closer inspection of the charge distribution for the antibonding mode in Figure 5b shows a slight depletion of the charge at the tip of the lower AR nanorod. This nondipolar charge polarization is a result of the admixture of higher multipolar primitive plasmon modes in the hybridized dimer modes.

Figure 5c,d depicts hybridization diagrams for the homo- and heterodimers. For the homodimer, the interactions are strong and the hybridized plasmon functions consist of equal contributions of plasmons from both nanorods. For the heterodimer, the interaction is a little weaker, resulting in smaller shifts of the hybridized states from the primitive (individual) nanorod modes (see insets). The bonding mode is dominated by the LSPR of the higher AR nanorod and the antibonding mode by the smaller AR nanorod. For simplicity, the hybridization schemes in Figure 5c,d only show the interactions between primitive dipolar plasmon modes.

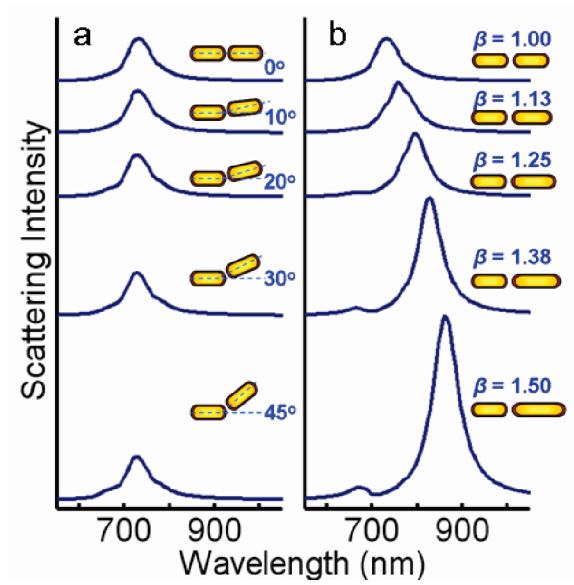

Figure 4. Integrated dark-field scattering spectra with (a) varying angular offset, δ, from a linear alignment and with (b) increasing $\beta = AR_2/AR_1$, *i.e.*, increasing the length of the right rod in increments of 10 nm. In panel (a), the rods are modeled having dimensions of 80 × 30 nm with a 4 nm thick dielectric coating and a 10 nm end-to-end gap size. In panel (b), the dimensions of the left rod are held constant at 80 × 30 nm, while the length of the right rod is varied. For comparison, the dimer studied in Figure 3 has $\delta = 10°$ and $\beta = 1.21$. All spectra are normalized to the peak intensity for the linear homodimer case.

The final validation of our mode assignments can be accomplished by rescaling the dimer from the quasistatic regime where an exact mode analysis can be performed to the actual size in the experiment. Figure 6a shows such FDTD simulations for a heterodimer with $\beta = 1.2$. As the size of the dimer is scaled up into the retarded regime, the plasmon modes are red-shifted and broadened. However, no new modes, no mode crossings, and no significant redistribution of spectral weights of the peaks result. Therefore the two modes in the actual heterodimer are indeed the ones inferred from the plasmon hybridization calculations. Figure 6b shows the normalized integrated dark-field scattering spectra for each of the scaled dimers. Because extinction includes absorption and scattering into all angles while scattering only includes backscattering within the experimental collection cone, the scattering intensity is much smaller than the extinction intensity.

Just as symmetry breaking can introduce new spectral features for a linear homodimer, bringing the rods into conductive contact also drastically modifies the optical properties of the dimer. Specifically, conductive

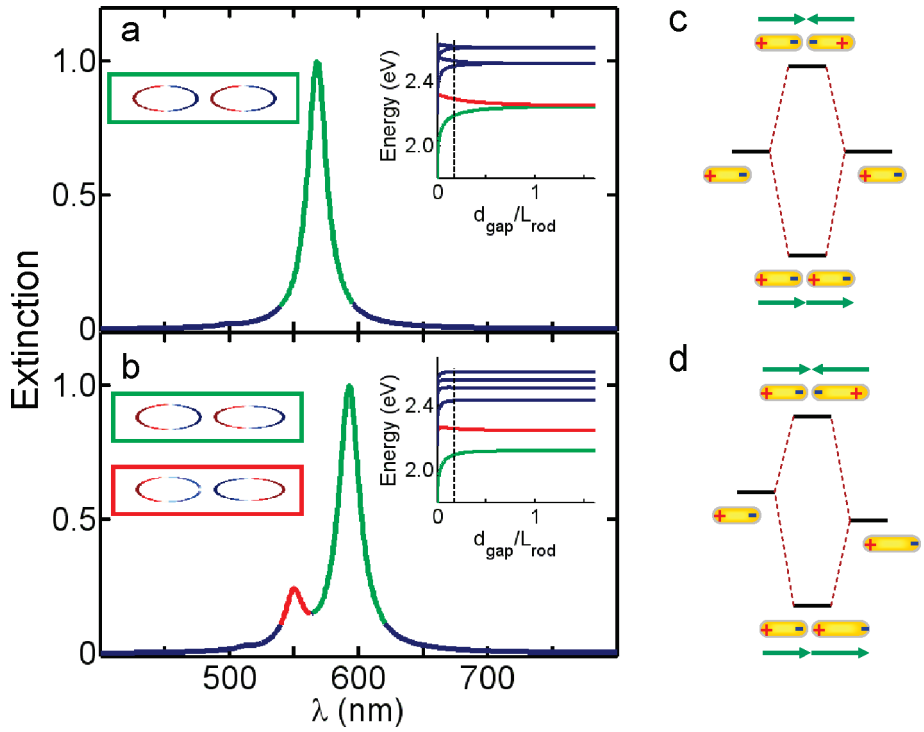

Figure 5. Extinction spectra calculated using plasmon hybridization theory for (a) a homodimer (β = 1) of prolate spheroids with major and minor axes of 14 and 5.6 nm and (b) a heterodimer (β = 1.2) consisting of a 14 × 5.6 nm, AR = 2.5 nm and a 15.2 × 5 nm, AR = 3 nm prolate spheroid. The interparticle distance was adjusted to 2.4 nm (dashed line in inset) to approximate d_{gap}/L_{rod} for the dimer shown in Figure 3, where d_{gap} is the size of the gap and L_{rod} denotes the length of one rod, the shorter one in the case of the heterodimer. The insets show how the eigenvalues of the bonding and antibonding combinations for the $l = 1-3$ primitive rod modes evolve as a function of the gap size. The charge distributions are shown for all visible peaks for each extinction spectrum: at 570 nm (2.19 eV) for the homodimer, and at 595 nm (2.09 eV) and 550 nm (2.25 eV) for the heterodimer. Diagrams illustrate the interactions of the primitive dipoles for the (c) homodimer and (d) heterodimer.

contact allows a dimer to support a charge transfer plasmon mode which involves both a continuous polarization of the charge distribution over both particles and an oscillating electric current across the junction between the two nanoparticles.[11,19] Figure 7 shows the spectra for a linear and bent (δ = 40°) touching dimer. The geometries are depicted in panels e and h, and the corresponding spectra are given in panels a and b. Both spectra exhibit a long wavelength rising feature, suggesting a peak beyond 1100 nm, the upper limit of the CCD spectrometer.

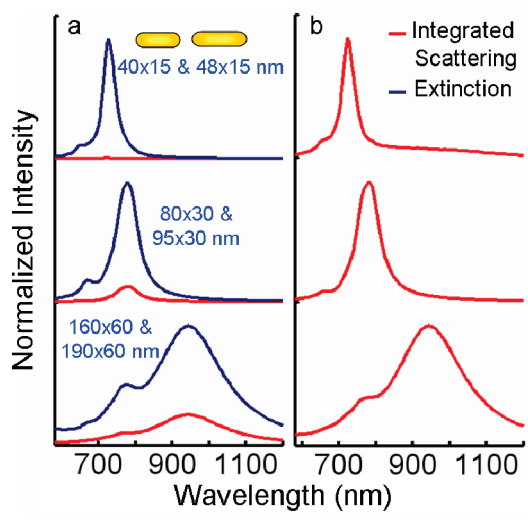

Figure 6. Calculated spectra for the heterodimer with β = 1.2 with different nanorod sizes from the quasistatic regime to dimensions similar to and larger than the experimental case. Spectra in (a) are normalized to the extinction, while each plot of integrated scattering simulated with the dark-field geometry is normalized to itself in (b).

It is very difficult, however, to confirm experimentally that the two nanorods are indeed touching. An SEM has limited resolution and could potentially melt the dimer at the highest magnification. To verify that the observed scattering spectrum results from metallic contact of the rods and not just an overlap of their dielectric coating, we resort to theoretical simulations. The inset in Figure 7a shows that the energy of the bonding mode red-shifted by ~160 nm when the environment in the junction was changed from vacuum ($\varepsilon = 1$) to CTAB ($\varepsilon = 4$). However, further increasing ε to an unrealistically high value of 8 only shifts the peak 30 nm to ~880 nm. This limited shift suggests that the nanorods are in conductive contact and that the low energy mode arises from the charge transfer plasmon.

Figure 7c shows the scattering spectra calculated for varying dimer separation and conductive overlap. As *d* decreases from 2 to 1 nm, the principal peak corresponding to the bonding dimer plasmon red shifts

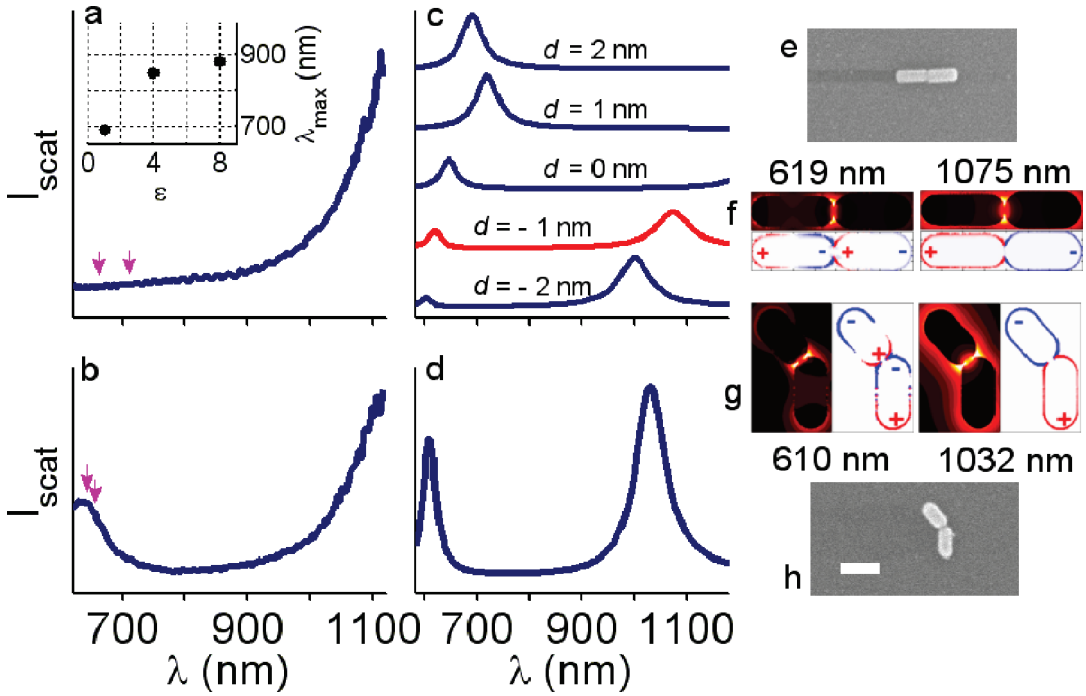

Figure 7. (a) Experimental unpolarized dark-field scattering spectrum of a linear dimer comprising rods with dimensions of (77 × 29) ± 5 nm (left) and (72 × 34) ± 5 nm (right) shown in the SEM image in (e). (b) Measured scattering spectrum of the bent dimer with δ = 40° in (h), comprising rods that are (72 × 38) ± 5 nm (top) and (78 × 38) ± 5 nm (bottom). The arrows in (a) and (b) indicate the predicted λ_{max} of the individual rods within each dimer based on the aspect ratio dependence in Figure 1b. The inset of (a) shows FDTD calculations of how λ_{max} of the dipole bonding mode evolves as a function of the dielectric constant of the material between a linear dimer with a 1 nm gap distance. The spectra in (c) are the integrated scattering intensities calculated by FDTD as a function of gap between the rods (d = 2, 1, 0, −1, −2 nm). A simulation of two particles in conductive contact with $d = -1$ nm and δ = 40° is shown in (d) to accompany (b). (f) Calculated electric field enhancement (top) and charge distribution (bottom) for the linear touching dimer with $d = -1$ nm (red curve in c) at 619 and 1075 nm. Likewise, (g) shows the electric field enhancement and charge distribution at 610 and 1032 nm for the bent touching dimer with $d = -1$ nm.

from 690 to 720 nm. When the rods begin to make conductive contact at $d = 0$ nm, the bonding plasmon mode blue shifts to 619 nm and a charge transfer plasmon appears at a wavelength beyond 1100 nm, which is not accessible with our detector. The sudden blue shift of the bonding plasmon mode for $d = 0$ is due to the interaction with the low energy charge transfer plasmon mode. With increasing conductive overlap, both resonances blue shift. This blue shift can be qualitatively understood from the dependence of the plasmon energies of individual nanorods on their aspect ratios. Making d more negative in the simulation corresponds to reducing the length of an almost continuous single nanorod structure. The charge transfer plasmon resembles a dipolar ($l = 1$) nanorod resonance, and the bonding dimer plasmon resembles an octupolar ($l = 3$) mode of a nanorod that, in this particular case, is approximately 150 × 30 nm. The interactions that occur for dimers with $d \leq 0$ result from conductive interactions between the particles and do not depend on the dielectric surrounding. We therefore omitted the CTAB coating in the simulations in Figure 7.

Comparing the series of simulated spectra in Figure 7c to the experimental scattering spectrum in Figure 7a shows that the best qualitative agreement is reached for an interparticle distance of $d = -1$ nm (red curve) for this linear touching dimer (Figure 7e). We have also performed extensive classical electromagnetic simulations for subnanometer separations. In this region, the capacitively coupled bonding dimer resonance red shifts monotonically with decreasing interparticle distance, as also shown in Figure 5. Within classical methods, shifting this mode beyond 1100 nm would require subangstrom separations.[45] At such small separations, however, quantum effects such as tunneling and screening would remove this mode, effectively resulting in a charge transfer plasmon.[26]

The bonding dimer plasmon is too weak to be observed experimentally in Figure 7a. Expanding the detection window to shorter wavelengths by changing the center wavelength of the grating from 950 to 650 nm did not yield an observable peak either. The energy and intensity of this mode depends strongly on d, as shown in Figure 7c, and also on the touching profile,[11] which is extremely difficult to access from the SEM images. A more detailed investigation of the touching profile for conductively coupled plasmons will be presented in a future study.

In contrast to the experimental spectrum of the linear dimer (Figure 7a), a simulation shown in Figure 7d of the bent touching dimer (Figure 7h) assuming a conductive overlap of $d = -1$ nm results in an excellent ac-

count of the experimental spectrum in Figure 7b. The intensity of the bonding dimer mode is strongly enhanced compared to the charge transfer plasmon in both experiment and simulation, presumably due to the significant angular offset. These results are consistent with a recent study on near-field imaging of the induced electric fields in touching and nearly touching nanocubes.[17] It should also be mentioned that conductive contact is unlikely to occur for rods aligned side-by-side because CTAB binds preferentially to the {100} sides of gold nanorods instead of the {111} ends, leaving the tips mostly unprotected and hence allowing much smaller end-to-end distances.[46]

The charge distributions calculated for $d = -1$ in the case of the linear, Figure 7f (right) at 1075 nm, and bent, Figure 7g (right) at 1032 nm, touching dimers both represent a dipole mode delocalized over the entire length of the dimer. This is typical for a charge transfer plasmon where the charge on each nanorod oscillates because of an alternating electric current across the junction. The higher energy modes at 619 nm (Figure 7f, left) and 610 nm (Figure 7g, left) for both heterodimers are essentially screened bonding dimer plasmon modes where the capacitive coupling has been reduced by electrically "short circuiting" the junction due to the metallic contact.

Mulvaney and co-workers have previously observed two LSPR peaks for end-to-end dimers of chemically prepared nanorods with smaller average diameters of 15 nm.[29] In particular, a strongly coupled linear dimer with nanorods of very similar size yielded two peaks, which were assigned to a lower energy dipolar bonding LSPR and a higher energy bonding multipolar mode which is expected to be optically active at small separations due to additional hybridization with primitive dipolar modes.[19,20] The antibonding mode was ruled out as the origin of the second higher energy peak due to the absence of two distinct peaks for a different linear dimer consisting of two very differently sized rods. As seen in Figures 4−6, such a dimer is expected to yield an observable antibonding mode in the nontouching configuration. Two modes can also arise from dimers with touching particles, but these modes are fundamentally different, as illustrated by the charge distributions in Figure 7f,g, especially for the lower energy charge transfer plasmon. However, it is nearly impossible to precisely determine the gap size and distinguish if the nanorods are touching given the resolution of SEM. The trends observed in this work, however, are consistent with recent studies of (barely) touching nanoparticles, which have specifically addressed spectral changes due to creating or modifying the conductive contact region, strongly suggesting that mixing of primitive rod modes does not sufficiently describe the optical response of nanostructures in the presence of metallic contact.[15−19]

CONCLUSIONS AND PROSPECTS

We have investigated the role of symmetry breaking and conductive overlap on the plasmon coupling in gold nanorod dimers through correlated SEM imaging, polarization-sensitive single-particle dark-field scattering spectroscopy and simulations using both FDTD and plasmon hybridization theory. In the FDTD calculations, we were able to match the experimental conditions very closely including the CTAB coating, glass substrate, and the excitation and collection geometries. Plasmon hybridization analysis enabled us to further verify the mode assignments. We found that symmetry breaking due to a size mismatch had the strongest effect on the collective plasmon modes. For a heterodimer, where a mirror plane in the junction is absent, antibonding dimer modes that would not be visible for a homodimer appear clearly in the spectrum. When a conductive overlap is present between the two particles, a low energy charge transfer plasmon mode appears prominently in the spectrum. These results are important for understanding the plasmonic properties of self-assembled aggregates of chemically synthesized nanoparticles which are prone to imperfections in the form of irregular spacings, random orientations, and inhomogeneous sizes of the individual nanoparticles. The trends established here can then be extended to more complex assemblies having a larger number of constituent nanoparticles, which are currently of special interest for plasmonic antennas, waveguides, and substrates for surface-enhanced spectroscopies.

The appearance of a distinct charge transfer plasmon in the optical spectrum of nanoparticle dimers opens new directions among plasmonic applications. In a recent fully quantum mechanical calculation of the optical properties of nanoparticle dimers, it was shown that conductive coupling can occur through electron tunneling even at dimer separations as large as 1 nm and does not require direct physical contact between the particles.[26] Using chemical linkers, it may be possible to control the width of the dimer junctions with (sub)nanometer accuracy. Furthermore, using conductive molecules as linkers may enable conductive coupling even for dimer separations beyond 1 nm. Dimers with small interparticle gaps present interesting experimental and theoretical challenges in plasmonics, which require further studies using higher resolution spatial imaging, direct mapping of the charge distributions for the different plasmon modes, and quantum mechanical modeling in addition to electromagnetic simulations. For larger, more realistic structures in close contact, quantum mechanical calculations would not be possible due to the large number of electrons. Instead, one would have to resort to classical electromagnetic calculations, such as FDTD, and modeling the individual nanoparticles using nonlocal dielectric functions.

METHODS

Dark-Field Scattering Spectroscopy. Individual gold nanorods and dimers deposited on patterned glass substrates were located exactly in both an SEM (FEI Quanta 400), operating in wet mode to offset charging on the nonconductive substrate, and a home-built single-particle spectrometer with a cooled Si CCD camera.[47] SEM images were typically taken at a magnification of 60 000, and the error in determining the nanoparticle size was about 5 nm. Dark-field excitation was performed in a reflected light geometry using an inverted microscope (Zeiss, Axiovert 200) with a halogen lamp as an excitation source. To allow for coarse and fine adjustments of the sample, a home-built sample holder was attached to a manual translational stage and mounted on an *xyz* piezo scanning stage (Physik Instrumente, P-517.3CL) connected to a surface probe microscope controller (RHK Technology, SPM 1000). Scattered light was collected using a Zeiss Epiplan-Neofluar 50×/0.8 objective and, after passing through a 50 μm pinhole and a polarizing beam splitter, focused onto two avalanche photodiode detectors (Perkin-Elmer, SPCM-AQR). Images were collected point by point by scanning the sample. We used filters of known optical density in the detection path as necessary to prevent saturating the detectors. Scattering spectra were acquired with a spectrometer (Princeton Instruments, Acton SP2150i) and a CCD camera (Princeton Instruments, PIXIS 400BR). When taking a spectrum, the scanning stage moved the sample to the desired location so that only the scattered light from the selected location could pass through the pinhole. The scattered light was directed to the entrance of the spectrometer using a motorized flipper mount (New Focus), dispersed by a grating (300 L/mm, blaze wavelength: 500 nm), and detected by the CCD camera. The spectra were averaged over six frames, each having an integration time of 30 s. The background was measured at a region with no nanoparticles present, dark counts were measured with the lamp off, and we corrected for the lamp and optical components by dividing by the spectrum of a white light reflectivity standard (Labsphere, SRS-99-010). A polarizer was placed in the detection path after the pinhole to measure the polarization dependence of the scattered light. A depolarizer followed the polarizer to avoid any polarization bias due to the spectrometer. The center wavelength of the grating was set to 650 nm. To extend the detection window to wavelengths beyond 1000 nm, the center wavelength was changed to 950 nm and a 610 nm long pass filter was inserted to remove secondary reflections by the spectrometer grating.

FDTD Simulations. Electromagnetic simulations of the plasmonic properties for the different nanorod dimer structures were carried out using the FDTD method. The gold metal was modeled using a Drude dielectric function with parameters fitted to the experimental data for gold. This fit provides an accurate description of the plasmonic properties of gold for wavelengths larger than 500 nm.[39] The individual nanorods were modeled as cylinders with two hemispherical end caps. The calculations included the detailed modeling of the geometry of the dark-field scattering microscope and also the glass substrate which was modeled as an infinitely thick dielectric layer of permittivity $\varepsilon = 2.31$.[37]

Plasmon Hybridization. The individual nanorods were modeled as prolate spheroids with aspect ratios defined as the ratio of their major to minor axes. The physical sizes of the dimers were scaled down to the quasistatic limit by dividing all dimensions by a common scaling factor. The calculations were carried out including all primitive nanorod plasmon modes up to multipolar order $l_{max} = 50$, although the calculations typically converged for $l_{max} = 15$. The dimers were assumed to be in vacuum, with each nanorod having a bulk plasmon frequency of $\omega_B = 8.95$ eV, a dielectric constant of $\varepsilon_\infty = 9.5$ representing the polarizable background of the metal, and an intrinsic damping of $\gamma = 0.069$ eV as appropriate for a Drude fit to the dielectric function of gold. The incident electrostatic field was polarized along the long axis of the dimers.

Acknowledgment. Support was provided by the Robert A. Welch Foundation (C-1664 to S.L., C-1222 to P.N.), 3M (Non-Tenured Faculty Grant to S.L.), NSF (CHE-0955286 to S. Link), and the Center for Advanced Solar Photophysics, an Energy Frontier Research Center funded by the U.S. Department of Energy (P.N.). L.S.S. acknowledges support from an NSF IGERT fellowship and Alexei Tcherniak for useful discussions.

Supporting Information Available: Scattering spectra at varying angles of the polarizing analyzer. This material is available free of charge *via* the Internet at http://pubs.acs.org.

REFERENCES AND NOTES

1. Link, S.; El-Sayed, M. A. Optical Properties and Ultrafast Dynamics of Metallic Nanocrystals. *Annu. Rev. Phys. Chem.* **2003**, *54*, 331–366.
2. Murphy, C. J.; Sau, T. K.; Gole, A. M.; Orendorff, C. J.; Gao, J.; Gou, L.; Hunyadi, S. E.; Li, T. Anisotropic Metal Nanoparticles: Synthesis, Assembly, and Optical Applications. *J. Phys. Chem. B* **2005**, *109*, 13857–13870.
3. Maier, S. A.; Atwater, H. A. Plasmonics: Localization and Guiding of Electromagnetic Energy in Metal/Dielectric Structures. *J. Appl. Phys.* **2005**, *98*, 11101.
4. Kelly, K. L.; Coronado, E.; Zhao, L. L.; Schatz, G. C. The Optical Properties of Metal Nanoparticles: The Influence of Size, Shape, and Dielectric Environment. *J. Phys. Chem. B* **2002**, *107*, 668–677.
5. Jain, P. K.; Huang, W.; El-Sayed, M. A. On the Universal Scaling Behavior of the Distance Decay of Plasmon Coupling in Metal Nanoparticle Pairs: A Plasmon Ruler Equation. *Nano Lett.* **2007**, *7*, 2080–2088.
6. Sönnichsen, C.; Reinhard, B. M.; Liphardt, J.; Alivisatos, A. P. A Molecular Ruler Based on Plasmon Coupling of Single Gold and Silver Nanoparticles. *Nat. Biotechnol.* **2005**, *23*, 741–745.
7. Wang, Z.; Levy, R.; Fernig, D. G.; Brust, M. The Peptide Route to Multifunctional Gold Nanoparticles. *Bioconjugate Chem.* **2005**, *16*, 497–500.
8. Huang, X.; El-Sayed, I. H.; Qian, W.; El-Sayed, M. A. Cancer Cells Assemble and Align Gold Nanorods Conjugated to Antibodies To Produce Highly Enhanced, Sharp, and Polarized Surface Raman Spectra: A Potential Cancer Diagnostic Marker. *Nano Lett.* **2007**, *7*, 1591–1597.
9. Jackson, J. B.; Halas, N. J. Surface-Enhanced Raman Scattering on Tunable Plasmonic Nanoparticle Substrates. *Proc. Natl. Acad. Sci. U.S.A.* **2004**, *101*, 17930–17935.
10. Alexander, K., D.; Hampton, M., J.; Zhang, S.; Dhawan, A.; Xu, H.; Lopez, R. A High-Throughput Method for Controlled Hot-Spot Fabrication in SERS-Active Gold Nanoparticle Dimer Arrays. *J. Raman Spectrosc.* **2009**, *40*, 2171–2175.
11. Romero, I.; Aizpurua, J.; Bryant, G. W.; Garcia de Abajo, F. J. Plasmons in Nearly Touching Metallic Nanoparticles: Singular Response in the Limit of Touching Dimers. *Opt. Exp.* **2006**, *14*, 9988–9999.
12. Tamaru, H.; Kuwata, H.; Miyazaki, H. T.; Miyano, K. Resonant Light Scattering from Individual Ag Nanoparticles and Particle Pairs. *Appl. Phys. Lett.* **2002**, *80*, 1826–1828.
13. Aizpurua, J.; Bryant, G. W.; Richter, L. J.; Garcia de Abajo, F. J.; Kelley, B. K.; Mallouk, T. Optical Properties of Coupled Metallic Nanorods for Field-Enhanced Spectroscopy. *Phys. Rev. B* **2005**, *71*, 235420–235413.
14. Dahmen, C.; Schmidt, B.; von Plessen, G. Radiation Damping in Metal Nanoparticle Pairs. *Nano Lett.* **2007**, *7*, 318–322.
15. Atay, T.; Song, J.-H.; Nurmikko, A. V. Strongly Interacting Plasmon Nanoparticle Pairs: From Dipole−Dipole Interaction to Conductively Coupled Regime. *Nano Lett.* **2004**, *4*, 1627–1631.
16. Danckwerts, M.; Novotny, L. Optical Frequency Mixing at Coupled Gold Nanoparticles. *Phys. Rev. Lett.* **2007**, *98*, 026104.
17. Kim, D.; Han, S. W.; Yun, W. S.; Kim, Z. H. Real-Space Mapping of the Strongly Coupled Plasmons of Nanoparticle Dimers. *Nano Lett.* **2009**, *9*, 3619–3625.
18. Kiristopuryan, A.; Ekinci, Y.; Giannini, R.; Sahoo, P. K.;

Gorodyska, G.; Loffler, J. F. High-Throughput Fabrication of Nanoantennae over Large Areas for Biosensing and Nanospectroscopy. *Appl. Phys. Lett.* **2009**, *95*, 231903.
19. Lassiter, J. B.; Aizpurua, J.; Hernandez, L. I.; Brandl, D. W.; Romero, I.; Lal, S.; Hafner, J. H.; Nordlander, P.; Halas, N. J. Close Encounters between Two Nanoshells. *Nano Lett.* **2008**, *8*, 1212–1218.
20. Rojas, R.; Claro, F. Electromagnetic Response of an Array of Particles: Normal-Mode Theory. *Phys. Rev. B* **1986**, *34*, 3730–3736.
21. Nie, Z.; Fava, D.; Kumacheva, E.; Zou, S.; Walker, G. C.; Rubinstein, M. Self-Assembly of Metal-Polymer Analogues of Amphiphilic Triblock Copolymers. *Nat. Mater.* **2007**, *6*, 609–614.
22. Sardar, R.; Shumaker-Parry, J. S. Asymmetrically Functionalized Gold Nanoparticles Organized in One-Dimensional Chains. *Nano Lett.* **2008**, *8*, 731–736.
23. Thomas, K. G.; Barazzouk, S.; Ipe, B. I.; Joseph, S. T. S.; Kamat, P. V. Uniaxial Plasmon Coupling through Longitudinal Self-Assembly of Gold Nanorods. *J. Phys. Chem. B* **2004**, *108*, 13066–13068.
24. deWaele, R.; Koenderink, A. F.; Polman, A. Tunable Nanoscale Localization of Energy on Plasmon Particle Arrays. *Nano Lett.* **2007**, *7*, 2004–2008.
25. Maier, S. A.; Kik, P. G.; Atwater, H. A.; Meltzer, S.; Harel, E.; Koel, B. E.; Requicha, A. A. G. Local Detection of Electromagnetic Energy Transport below the Diffraction Limit in Metal Nanoparticle Plasmon Waveguides. *Nat. Mater.* **2003**, *2*, 229–232.
26. Zuloaga, J.; Prodan, E.; Nordlander, P. Quantum Description of the Plasmon Resonances of a Nanoparticle Dimer. *Nano Lett.* **2009**, *9*, 887–891.
27. Brown, L. V.; Sobhani, H.; Lassiter, J. B.; Nordlander, P.; Halas, N. J. Heterodimers: Plasmonic Properties of Mismatched Nanoparticle Pairs. *ACS Nano* **2010**, *4*, 819–832.
28. Jain, P. K.; Eustis, S.; El-Sayed, M. A. Plasmon Coupling in Nanorod Assemblies: Optical Absorption, Discrete Dipole Approximation Simulation, and Exciton-Coupling Model. *J. Phys. Chem. B* **2006**, *110*, 18243–18253.
29. Funston, A. M.; Novo, C.; Davis, T. J.; Mulvaney, P. Plasmon Coupling of Gold Nanorods at Short Distances and in Different Geometries. *Nano Lett.* **2009**, *9*, 1651–1658.
30. Pramod, P.; Thomas, K. G. Plasmon Coupling in Dimers of Au Nanorods. *Adv. Mater.* **2008**, *20*, 4300–4305.
31. Tabor, C.; Van Haute, D.; El-Sayed, M. A. Effect of Orientation on Plasmonic Coupling between Gold Nanorods. *ACS Nano* **2009**, *3*, 3670–3678.
32. Gluodenis, M.; Foss, C. A. The Effect of Mutual Orientation on the Spectra of Metal Nanoparticle Rod−Rod and Rod−Sphere Pairs. *J. Phys. Chem. B* **2002**, *106*, 9484–9489.
33. Shao, L.; Woo, K. C.; Chen, H.; Jin, Z.; Wang, J.; Lin, H.-Q. Angle- and Energy-Resolved Plasmon Coupling in Gold Nanorod Dimers. *ACS Nano* **2010**, *4*, 3053–3062.
34. Sönnichsen, C.; Alivisatos, A. P. Gold Nanorods as Novel Nonbleaching Plasmon-Based Orientation Sensors for Polarized Single-Particle Microscopy. *Nano Lett.* **2005**, *5*, 301–304.
35. Chang, W.-S.; Ha, J. W.; Slaughter, L. S.; Link, S. Plasmonic Nanorod Absorbers as Orientation Sensors. *Proc. Natl. Acad. Sci. U.S.A.* **2010**, *107*, 2781–2786.
36. Shibu Joseph, S. T.; Ipe, B. I.; Pramod, P.; Thomas, K. G. Gold Nanorods to Nanochains: Mechanistic Investigations on Their Longitudinal Assembly Using α,ω-Alkanedithiols and Interplasmon Coupling. *J. Phys. Chem. B* **2006**, *110*, 150–157.
37. Wu, Y.; Nordlander, P. Finite-Difference Time-Domain Modeling of the Optical Properties of Nanoparticles near Dielectric Substrates. *J. Phys. Chem. C* **2009**, *114*, 7302–7307.
38. Abate, Y.; Schwartzberg, A.; Strasser, D.; Leone, S. R. Nanometer-Scale Size Dependent Imaging of Cetyltrimethylammonium Bromide (CTAB) Capped and Uncapped Gold Nanoparticles by Apertureless Near-Field Optical Microscopy. *Chem. Phys. Lett.* **2009**, *474*, 146–152.
39. Oubre, C.; Nordlander, P. Optical Properties of Metallodielectric Nanostructures Calculated Using the Finite Difference Time Domain Method. *J. Phys. Chem. B* **2004**, *108*, 17740–17747.
40. Oubre, C.; Nordlander, P. Finite-Difference Time-Domain Studies of the Optical Properties of Nanoshell Dimers. *J. Phys. Chem. B* **2005**, *109*, 10042–10051.
41. Jackson, J. D. *Classical Electrodynamics*, 2nd ed.; John Wiley & Sons, Inc.: New York, 1975.
42. Nordlander, P.; Oubre, C.; Prodan, E.; Li, K.; Stockman, M. I. Plasmon Hybridization in Nanoparticle Dimers. *Nano Lett.* **2004**, *4*, 899–903.
43. Willingham, B. A.; Brandl, D. W.; Nordlander, P. Plasmon Hybrization in Nanorod Dimers. *Appl. Phys. B: Lasers Opt.* **2008**, *93*, 209–216.
44. Chu, M.-W.; Myroshnychenko, V.; Chen, C. H.; Deng, J.-P.; Mou, C.-Y.; Garcia de Abajo, F. J. Probing Bright and Dark Surface-Plasmon Modes in Individual and Coupled Noble Metal Nanoparticles Using an Electron Beam. *Nano Lett.* **2009**, *9*, 399–404.
45. Marhaba, S.; Bachelier, G.; Bonnet, C.; Broyer, M.; Cottancin, E.; Grillet, N.; Lerme, J.; Vialle, J.-L.; Pellarin, M. Surface Plasmon Resonance of Single Gold Nanodimers near the Conductive Contact Limit. *J. Phys. Chem. C* **2009**, *113*, 4349–4356.
46. Johnson, C. J.; Dujardin, E.; Davis, S. A.; Murphy, C. J.; Mann, S. Growth and Form of Gold Nanorods Prepared by Seed-Mediated, Surfactant-Directed Synthesis. *J. Mater. Chem.* **2002**, *12*, 1765–1770.
47. Chang, W.-S.; Slaughter, L. S.; Khanal, B. P.; Manna, P.; Zubarev, E. R.; Link, S. One-Dimensional Coupling of Gold Nanoparticle Plasmons in Self-Assembled Ring Superstructures. *Nano Lett.* **2009**, *9*, 1152–1157.